Catalysis Science & Technology

ROYAL SOCIETY OF CHEMISTRY

PAPER

View Article Online
View Journal | View Issue

Cite this: *Catal. Sci. Technol.*, 2024, **14**, 1052

CO_2 chemisorption and activation on carbon nitride with less amino groups boost CO_2 photoreduction†

Debin Zeng, ‡ Xiting Wang, ‡ Chunguang Kuai, Zhuo Jiang* and Yuzheng Guo *

Received 15th November 2023,
Accepted 16th January 2024

DOI: 10.1039/d3cy01585h

rsc.li/catalysis

CO_2 chemisorption and activation are two crucial factors that can significantly impact the overall CO_2 conversion efficiency. However, achieving effective modulation of these processes in metal-free photocatalysts has proven to be challenging. In this study, we present a novel approach for activating CO_2 molecules by selectively removing some amino groups at the boundary of carbon nitride (CN). By doing so, we observed a concentration of photogenerated electrons at the nitrogen atoms neighboring the eliminated $-NH_2$ group. This electron concentration enhances the chemisorption and activation of CO_2, resulting in lowered energy barriers for the rate-determining step from CO_2 to *COOH. Interestingly, we found that only the nitrogen atoms adjacent to the removed $-NH_2$ group in CN serve as catalytic sites, in contrast to all the nitrogen atoms neighboring the $-NH_2$ group in CN–NH_2. As a result, CN exhibits superior catalytic efficiency, with a turnover frequency (TOF) for CO that is 23.11 times higher than that of CN–NH_2 under identical conditions.

1 Introduction

Solar-driven CO_2 reduction is a promising way to address both environmental and energy shortage issues.[1–3] Despite significant efforts over the past few decades, the conversion efficiency of this process has remained unsatisfactory. A key challenge in developing catalysts with high CO_2 conversion efficiency lies in the limited chemisorption ability of CO_2, coupled with the high activation energy required for CO_2 molecules to react on catalyst surfaces.[4–6] Consequently, addressing and enhancing these two aspects play crucial roles in promoting CO_2 photoreduction reactions.

Recently, various strategies have been employed to enhance the photoelectric conversion efficiency by improving the separation efficiency of photogenerated carriers. These strategies include the loading of co-catalysts and the construction of heterojunctions. However, the chemisorption and activation of CO_2, which are influenced by the size and type of transition metals, are often overlooked due to the challenges associated with detecting these processes at the molecular level. Green *et al.* reported that the size of Pt_n^- clusters plays a dominant role in both CO_2 chemisorption and activation efficiency.[7] Additionally, Weber *et al.* found that metal anions can affect CO_2 chemisorption and activation performance through gas-phase complexation between CO_2 and metal anions.[8]

Apart from the size and type of transition metals, electron redistribution on catalytic sites can also modify the CO_2 chemisorption and activation process. For instance, in a study by Cao *et al.*, electron transfer from an Au atom to a Cd vacancy led to the redistribution of electrons in CdS, resulting in a strong CO_2 chemisorption and activation ability. On the other hand, when an Au atom was anchored at an S vacancy, this electron transfer process was prevented, causing CO_2 molecules to only physically adsorb at the catalytic sites, even under the same CO_2 atmosphere.[9] Therefore, the modulation of the charge distribution of catalytic sites is significant for improving CO_2 chemisorption and activation, particularly in the context of non-metallic catalysts.

Since the initial report by Wang *et al.* on the ability of C_3N_4 to generate hydrogen under light illumination,[10] this

School of Electrical Engineering and Automation, Wuhan University, Wuhan, 430072, PR China. E-mail: zhuojiang@whu.edu.cn, yguo@whu.edu.cn

† Electronic supplementary information (ESI) available: XPS of Br 3d, XRD spectra, Raman spectra, EPR spectra, table of peak areas of C–N–H, N–$(C)_3$ and C–N=C based on XPS, table of peak areas of NH and NH_2 groups based on ^1H MAS NMR, SEM, TEM, HRTEM, STEM, pore size distribution, nitrogen adsorption–desorption isotherm, summary table of BET specific surface areas, pore sizes, and nanoparticle sizes, CO_2 adsorption isotherms, photocatalytic performance, comparison table of photocatalytic performance, redox potential, UV-vis DRS, EIS, time-resolved transient fluorescence decay spectra, transient photocurrent response, photovoltage, thermogravimetry analysis, CO_2 mass spectra, and table of peak areas of adsorbed H_2O, carbonates and adsorbed CO_2 based on XPS. See DOI: **https://doi.org/10.1039/d3cy01585h**

‡ These authors contributed equally to this work.

material has attracted significant research attention in subsequent decades. The interest in C_3N_4 stems from its favourable band structure and adjustable functionalities.[11–14] In this particular study, we synthesized carbon nitride (CN–NH_2) and its derivative, CN, by precisely removing certain –NH_2 groups from CN–NH_2. This coordination defect caused electron accumulation around the nitrogen catalytic sites adjacent to the lost –NH_2 group, resulting in a much higher negative charge density in these sites. Due to electron redistribution, the catalytic sites were regarded as Lewis basic sites for CO_2 chemisorption and activation, thus boosting CO_2 photoreduction under mild conditions.

2 Experimental details

Synthesis of CN–NH_2

Specifically, 1 g of $C_3H_6N_6$ was placed into a muffle furnace, heated to 500 °C at a heating rate of 2 °C min^{-1}, and maintained at this temperature for 4 h. The obtained material was termed as CN–NH_2.

Synthesis of CN

In a typical synthesis, 2 g of hexadecyl trimethyl ammonium bromide (CTAB) was dissolved in a mixed solution of cyclohexane, 1-pentanol and deionized water, and its total volume was 60 mL. This mixture was stirred for 30 min. Next, 1 g melamine was added into the mixed solution, and the pH was adjusted to 2 using HNO_3 with stirring. The resulting mixture was stirred for 1 h and transferred to a 100 mL Teflon autoclave, where it was heated at 160 °C for 16 h. The synthesized prepolymer was washed with anhydrous ethanol and deionized water 10 times each, subsequently dried at 60 °C for 10 h, and finally placed in a tube furnace. The prepolymer was heated to 500 °C at a heating rate of 2 °C min^{-1} under a 100 sccm argon flow and maintained at this temperature for 4 h. The obtained material was termed as CN. In CN, no bromine element was detected in X-ray photoelectron spectroscopy (XPS), suggesting the absence of residual bromine (Fig. S1†). Additionally, the results obtained from energy dispersive X-ray spectroscopy (EDS) showed negligible levels of bromine, further confirming its absence (Fig. S2†). To investigate the influence of CTAB, pH condition, solvothermal time, and temperature on the properties of CN, controlled experiments were conducted. CTAB, a cationic surfactant, carries a positive charge in aqueous solution. Due to its strong interaction, CTAB cations can react with the –NH_2 groups of melamine, resulting in the partial removal of –NH_2 groups of melamine.[15,16]

Characterization

X-ray diffraction (XRD) patterns were recorded using an XPert Pro X-ray diffractometer with Cu Kα radiation (λ = 1.54 Å). Fourier transform infrared (FTIR) spectra were obtained on a Thermo FTIR5700 Spectrometer. Raman spectra were recorded on a RENISHAW inVia Raman Microscope equipped with a 780 nm laser. Room temperature electron paramagnetic resonance (EPR) spectra were obtained on a JEOL ESR spectrometer (JES-FA200). XPS analyses were conducted using an ESCALAB250Xi with Al Kα radiation. The molar loss of nitrogen and hydrogen elements was detected using a vario EL III elemental analyzer. Field-emission scanning electron microscopy (FESEM) images were obtained on a Zeiss SIGMA. Scanning transmission electron microscopy (STEM) and elemental mapping were conducted on a JEM-F200 transmission electron microscope operating at an acceleration voltage of 200 kV. The N_2 adsorption/desorption isotherms, porosity and CO_2 adsorption isotherms were studied using an automatic analyzer (ASAP 2020). UV-vis diffuse reflectance spectra (DRS) were obtained using a UV-vis spectrophotometer (Shimadzu UV-2600) equipped with an integrating sphere detector. The EIS Nyquist plots, transient photocurrent response and Mott–Schottky curves were obtained on an electrochemical workstation (CHI760E). Time-resolved fluorescence spectra were recorded on a single photon counting module (PicoQuant, PMA Hybrid), which was excited using a 405 nm pulse laser. The zeta potentials of the synthesized materials were collected using a Zetasizer Nano ZSP.

In situ FTIR spectra of CO_2 photoreduction

In situ FTIR spectra of CO_2 photoreduction were acquired using a Thermo Scientific Nicolet iS50 spectrometer equipped with an *in situ* diffuse reflectance accessory cell. The sample was filled and compacted in the sample cell, and argon gas was introduced into the *in situ* cell to remove impurities. CO_2 and H_2O were subsequently introduced into the *in situ* cell, and the system was allowed to equilibrate for 30 min to ensure that the adsorption and desorption of the gases reached equilibrium. Prior to light irradiation, an FTIR spectrum was collected to establish the background, including catalyst and CO_2/H_2O information.

In situ FTIR spectra of CO_2 chemisorption

A 100 mg sample was subjected to 500 °C in a 5% H_2/Ar air flow for 1 h to desorb the adsorbed impurities. The sample was subsequently cooled to 100 °C, followed by the introduction of argon gas into the *in situ* cell to purge H_2. A background spectrum of the catalyst information was obtained prior to collecting the spectra upon the introduction of a 10% CO_2/Ar air flow into the *in situ* cell.

CO_2 temperature-programmed desorption and mass spectra

A 100 mg sample was heated to 500 °C in a helium air flow for 1 h to remove adsorbed impurities. After cooling to 50 °C, the sample was subjected to CO_2 in a temperature-programmed chemisorption instrument for 30 min, allowing the chemical adsorption of CO_2 on the catalyst. Subsequently, gaseous CO_2 was purged from the system with a helium air flow for 30 min. The temperature of the sample was then increased at a rate of 10 °C min^{-1} while collecting the CO_2

temperature-programmed desorption signal. The desorbed CO_2 from the temperature-programmed chemisorption instrument was further analyzed by mass spectrometry.

CO_2 photoreduction test

Photocatalytic tests for all samples were conducted using a Labsolar-6A system (Beijing Perfectlight) equipped with a 300 W Xe lamp (Beijing Perfectlight, PLS-SXE300, 320–780 nm, 1.50 W cm^{-2}). For the photocatalytic performance test, 20 mg of photocatalyst was dispersed in deionized water and dried in a quartz reactor at 60 °C overnight. To provide protons and act as a hole scavenger, 2 mL of deionized water was injected into the quartz reactor. Prior to irradiation, the reactor was pumped to a vacuum three times, and then filled with high-purity CO_2 gas to 70 kPa. Following a 3 h irradiation period, gas products were collected and analyzed using a gas chromatograph (Fuli, GC 9790 II) equipped with flame ionization and thermal conductivity detectors.

Calculation details

The first-principles calculations were performed on the Vienna *Ab initio* Simulation Package (VASP).[17] The interaction between ions and valance electrons was described by utilizing projector augmented wave (PAW) potentials while the exchange correlation energy was obtained by generalized gradient approximation.[18,19] Furthermore, the DFT-D_2 correction was included to evaluate the van der Waals interactions. The cutoff energy and Brillouin zone were 400 eV and 2 × 2 × 1 sheet *k*-point mesh, respectively. The convergence process of structure relaxations would be ceased when the conventional energy and force were 10^{-5} eV and 0.03 eV $Å^{-1}$, respectively. CN–NH_2 and CN had a vacuum layer of 15 Å placed above the surface slab.

The adsorption energy (E_{ad}) defined the interaction between intermediates and the surface, which was defined as $E_{ad} = E_{ads} + E_{sur} - E_{sys}$, where E_{ads} is the adsorbate energy prior to adsorption, E_{sur} is the surface energy prior to adsorption and E_{sys} is the system energy after adsorption. Gibbs free energies for gaseous and adsorbed intermediates were calculated at 298.15 K based on the expression $G_E = E_{DFT} + E_{ZEP} - TS$, where E_{DFT} is the electronic energy calculated by VASP, E_{ZEP} is the zero-point energy and TS is entropy contribution.[20]

3 Characterization results

Structural characterization

The X-ray diffraction (XRD) patterns of both CN–NH_2 and CN showed a good match with that of the hexagonal g-C_3N_4 (JCPDS card No. 087-1526), which corresponds to carbon nitride with a graphitic-like phase (Fig. 1a and S3†). In the XRD pattern, the diffraction peak centered at 2θ = 12.9° corresponds to the (100) plane, which represents the intralayer repeating units of heptazine heteroatoms with the –NH_2 group.[21] Additionally, another diffraction peak observed at 2θ = 27.2° corresponds to the (002) plane, which indicates the interlayer periodic stacking similar to graphite. Importantly, it was observed that both the (100) and (002) planes of CN were shifted to lower angles compared to CN–NH_2. This shift can be attributed to the absence of the –NH_2 group, which weakens the interlayer stacking, as reported in previous studies.[22,23]

To confirm the absence of the –NH_2 group in CN, Fourier transform infrared reflection (FTIR) spectra were used to analyze CN–NH_2 and CN in the spectral range of 3600–500 cm^{-1} (Fig. 1b). In the FTIR spectra, clear N–H stretching vibration signals were observed at 3428 and 3491 cm^{-1}, indicating the presence of the –NH_2 group in CN–NH_2.[21,24] However, in the CN spectra, these signals were significantly weakened, suggesting the loss of the –NH_2 group. This observation confirms that the –NH_2 groups were successfully removed from the CN material.

Furthermore, other characteristic peaks were analyzed in the FTIR spectra. The peak at 809 cm^{-1} corresponds to the stretching vibration of the triazine ring, while the peaks at 1240, 1324, 1414, and 1560 cm^{-1} represent the stretching vibration of aromatic heterocycles.[25–27] The presence of these peaks in the CN spectra indicates that the removal of the –NH_2 group did not damage the main structure of the material. This suggests that the structural integrity of the CN material was maintained even after the removal of the –NH_2 groups. These FTIR spectral analyses provide strong evidence for the absence of –NH_2 groups in the CN material and demonstrate that the removal of these groups did not adversely affect the main structure of the material. The preservation of aromatic heterocycles in CN was also confirmed by Raman spectroscopy, which displayed the increased signal intensities of aromatic heterocycles relative to CN–NH_2 (Fig. S4†). This unambiguously revealed that the removal of the –NH_2 group did not damage the main structure. Moreover, electron paramagnetic resonance (EPR) confirmed a strong EPR signal at g = 2.003 for CN compared with CN–NH_2, unambiguously unveiling the presence of unpaired electron signals caused by the removal of the –NH_2 group (Fig. 1c and S5†).[28,29]

Previous studies revealed that the removal of the –NH_2 group in carbon nitride would boost the electron migration from the bulk phase to the surface.[22,30] Therefore, accurately quantifying the loss percentage of –NH_2 groups in the CN structure was crucial. As shown in the XPS spectra (Fig. 1d and Table S1†), the content of C–N–H in CN decreased obviously compared with CN–NH_2, demonstrating the successful removal of –NH_2 groups. Moreover, magic angle spinning nuclear magnetic resonance (MAS NMR) experiments, employing C-labeled samples, confirmed the preservation of the primary structure as evidenced by the unaltered N–C═N (~163.5 ppm) and N═C–N_2 (~154.5 ppm) groups (Fig. 1e).[31] In contrast, MAS NMR experiments utilizing H-labeled samples demonstrated a substantial decrease in the peaks corresponding to the NH (~8.9 ppm) and NH_2 (~4.6 ppm) groups after the removal of the –NH_2

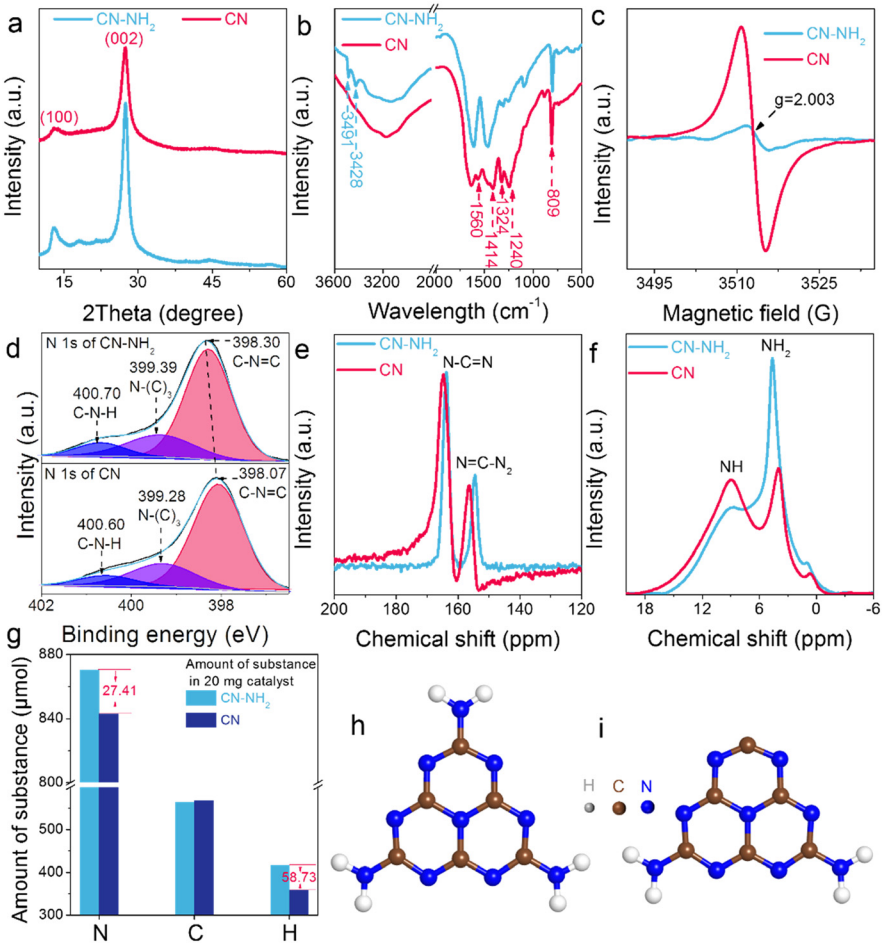

Fig. 1 Phase and structural characterization of synthesized samples. a) X-ray diffraction (XRD) patterns. b) Fourier transform infrared reflection (FTIR) spectra. c) Electron paramagnetic resonance (EPR) spectra. d) X-ray photoelectron spectra (XPS) of N 1s. e) Solid-state ^{13}C magic angle spinning nuclear magnetic resonance (MAS NMR) spectra. f) Solid-state ^{1}H MAS NMR spectra. g) The elemental content comparison between CN and CN–NH_2 for confirming the –NH_2 loss. The minimum units of atomic structures of h) CN–NH_2 and i) CN.

group (Fig. 1f).[31] By precisely fitting the peak areas of CN–NH_2 and CN independently in the MAS spectra, the percentage of NH_2 was observed to decrease from 59.45% (CN–NH_2) to 26.58% (CN) (Table S2†), surpassing the reduction observed in the XPS results, likely attributable to the surface and bulk disparities. Additionally, elemental analysis was performed to quantitatively determine the nitrogen and hydrogen element losses in CN. The loss of N and H in the CN sample was determined to be 27.41 and 58.73 μmol, respectively, with a nitrogen-to-hydrogen ratio close to 1 : 2, affirming the loss of –NH_2 groups (Fig. 1g). Notably, the –NH_2 loss in CN was calculated to be 14.07% based on the –NH_2 content criterion in CN–NH_2. These results, in conjunction with the aforementioned measurements, provided a detailed atomic structure of CN–NH_2 and CN, as depicted in Fig. 1h and i, respectively.

Morphology characterization

The synthesis of CN with a porous framework was accomplished through a solvothermal treatment and subsequent one-step calcination process (Fig. 2a). The elemental mapping images in Fig. 2b and c confirmed the uniform distribution of carbon and nitrogen elements in CN after the removal of the –NH_2 group. The CN construct exhibited a porous framework structure, as revealed by field-emission scanning electron microscopy (FESEM), transmission electron microscopy (TEM), and scanning transmission electron microscopy (STEM) analysis (Fig. 2d–g and S6–S8†). The pore size (4.5 to 52 nm) measured from the TEM image indicated the presence of mesopores in CN (Fig. S9†). The nitrogen adsorption–desorption isotherms and pore size distribution analysis suggested that both CN–NH_2 and CN exhibited mesopores. Moreover, it was found that the pore size of CN is larger than that of CN–NH_2, further confirming the successful removal of –NH_2 in CN (Fig. S10†). Notably, the inserted figure showed that the pore size of CN ranged from 3 to 50 nm, consistent with the pore size distribution results measured in the TEM image. The nanoparticle size of CN ranged from 160 to 710 nm, which was in sharp contrast with the nanoparticle size of CN–NH_2, ranging from 1030 to 4160 nm (Table S3†). This significant difference in size can be attributed to the presence

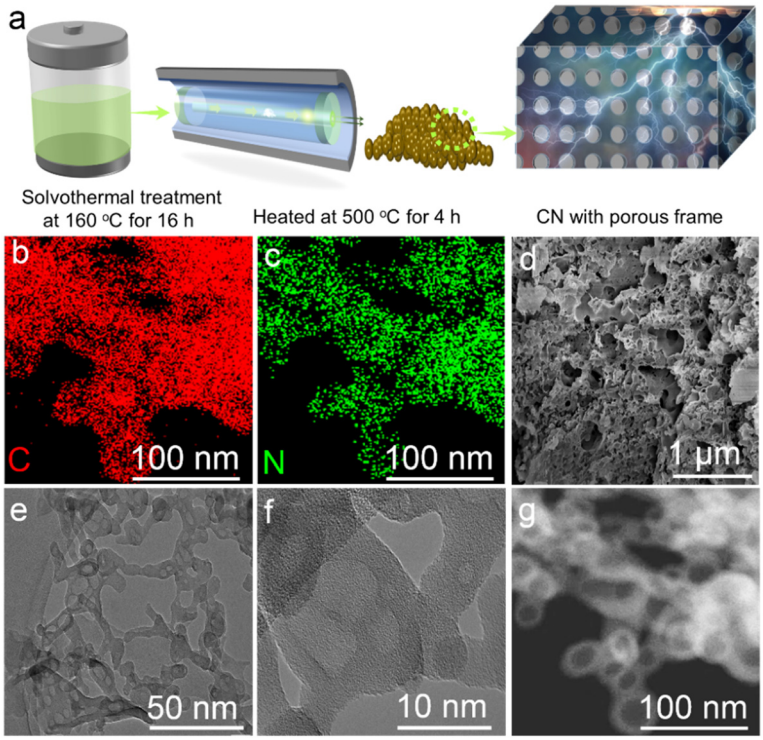

Fig. 2 Physical morphology of CN with a porous frame. a) The synthesis process of CN with a porous frame. Elemental mapping: b) carbon element and c) nitrogen element. d) Field-emission scanning electron microscopy (FESEM) image. e and f) Transmission electron microscopy (TEM) images. g) Scanning transmission electron microscopy (STEM) image.

of $-NH_2$ groups on the CN–NH_2 surface. Additionally, the porous structure and smaller nanoparticle size of CN contributed to its significantly improved BET specific surface area of 10.51 $m^2\ g^{-1}$, which was 5.2 times greater than that of CN–NH_2 (Table S4†). Furthermore, the removal of the $-NH_2$ group enhanced the CO_2 adsorption capacity, with CN demonstrating nearly 242% higher CO_2 adsorption compared to CN–NH_2, as depicted in Fig. S11.†

CO_2 photoreduction performance

The CO_2 photoreduction performance of CN–NH_2 and CN was assessed in a gas–solid system without the use of sacrificial agents or photosensitizers. To investigate the dependence of photocatalytic performance on catalyst mass, we conducted photocatalytic tests using CN with catalyst masses ranging from 0 to 65 mg (Fig. S12†). The results indicated a gradual enhancement of photocatalytic performance with increasing catalyst mass. We determined that a catalyst mass of 20 mg was appropriate, as it struck a balance between photocatalytic performance and the rationalized utilization cost of the catalyst. As depicted in Fig. 3a and S13.† CN–NH_2 exhibited CH_4 and CO production rates of 1.67 and 18.07 μmol $g^{-1}\ h^{-1}$. In contrast, CN displayed CH_4 and CO production rates of 1.44 and 58.83 μmol $g^{-1}\ h^{-1}$. The CO production rate of CN (58.83 μmol $g^{-1}\ h^{-1}$) was 3.26 times higher than that of CN–NH_2 (18.07 μmol $g^{-1}\ h^{-1}$), while the CO selectivity of CN (97.61%) exceeded that of CN–NH_2 (91.52%) (Fig. S14†). As shown in Fig. 3b, under visible light illumination, the CO_2 reduction performance of CN was enhanced, resulting in a CO production rate of 21.61 μmol $g^{-1}\ h^{-1}$, which was 5.61 times higher than that of CN–NH_2 (3.85 μmol $g^{-1}\ h^{-1}$). Notably, its conversion rate and selectivity surpassed those of some recently reported photocatalysts in CO_2 photoreduction (Table S5†), underscoring the superior application potential of the photocatalyst investigated in this study. Additionally, we evaluated the photocatalytic performance of CN by substituting CO_2 with argon (Fig. 3a). The results indicated the presence of only trace amounts of CO, confirming that the products may have originated from the catalytic process. This finding was further supported by an isotope tracer experiment using $^{13}CO_2$ instead of $^{12}CO_2$, which solely detected signals of $^{13}CH_4$ (m/z = 17) and ^{13}CO (m/z = 29) under identical conditions, providing clear evidence that both CH_4 and CO originated from CO_2 molecules rather than the decomposition of the photocatalyst itself (Fig. 3c). The detection of the $^{16}O_2$ and $^{18}O_2$ signals indicated that the generated holes were involved in the oxidation of H_2O, leading to the production of O_2 (Fig. 3c and S15†). This process was accompanied by the generation of $^{\cdot}OH$ (hydroxyl radicals) as well (Fig. S16†). Both O_2 and $^{\cdot}OH$ contribute to balancing the consumption of electrons and holes in the photocatalytic system. In addition to its significantly improved CO_2 reduction performance, the stability of CN was investigated after five consecutive cycles. Only a slight

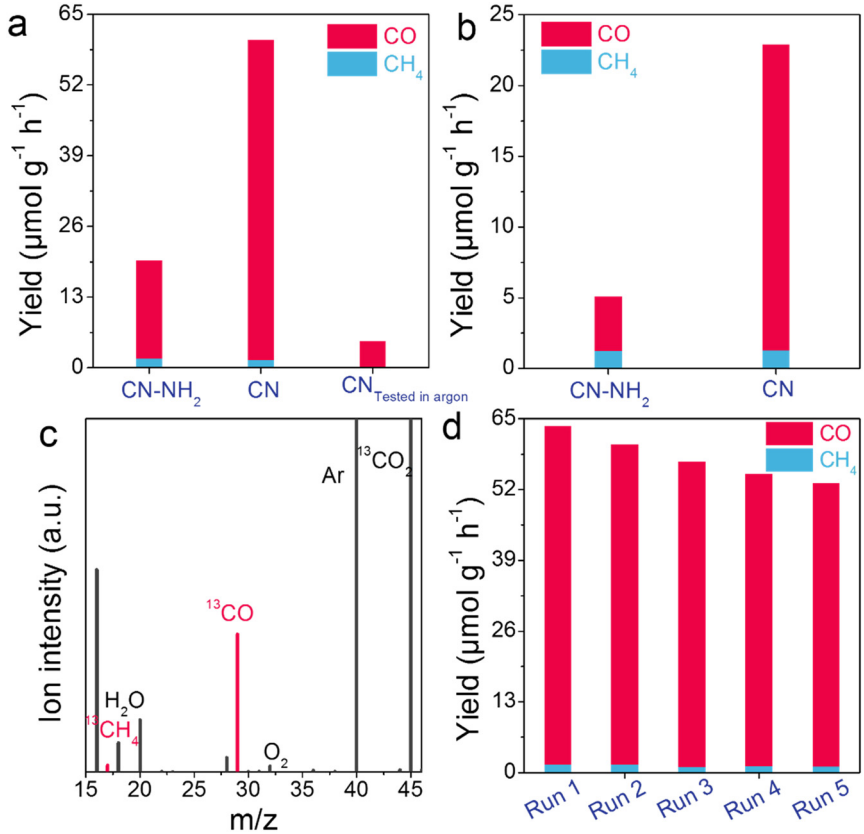

Fig. 3 CO_2 photoreduction performance. a) Photocatalytic performance of CN–NH_2 and CN. b) Photocatalytic performance obtained under visible light. c) The isotope tracer experiment of $^{13}CO_2$ photoreduction. d) Cycling tests of CO_2 photoreduction on CN (the reactor was evacuated and refilled with new H_2O and CO_2 for the next cycling test).

deactivation of 16.64% was observed during the final cycle, indicating reliable photocatalytic stability (Fig. 3d). This finding was consistent with the unchanged XRD peaks observed in Fig. S17,† clearly demonstrating that CN could be regarded as an exceptional catalyst for CO_2 reduction. To investigate the influence of light intensity, the apparent quantum yield (AQY) was further explored. The AQYs at 350, 365, 420, and 550 nm were determined to be 0.37, 0.19, 0.072, and 0.019%, respectively (Fig. S18†), aligning well with its light absorption curve, thereby indicating that the photocatalytic performance stemmed from its light absorption capacity.

Mechanism discussion of CO_2 photoreduction performance enhancement

The band structures of CN–NH_2 and CN were investigated using Mott–Schottky analysis and UV-vis diffuse reflectance (UV-vis DRS) spectroscopy, as shown in Fig. S19† and 4a, respectively. Both materials exhibited redox potentials that were suitable for CO_2 reduction and H_2O oxidation. Previous studies have indicated that the efficiency of CO_2 chemisorption and activation is influenced by the electron density at the catalytic site.[9,32–35] Therefore, it is crucial to comprehensively evaluate the electron density at the catalytic sites of CN–NH_2 and CN. This evaluation requires an examination of the light absorption capacity and charge separation efficiency, as these factors govern the electron density in the catalytic sites. In the following section, we will gradually investigate these aspects.

As depicted in Fig. 4a and S20,† CN exhibited superior light harvesting ability in both UV and visible light regions, accompanied by a noticeable reduction in the band gap from 2.64 eV (CN–NH_2) to 2.38 eV (CN). This signified that the removal of the –NH_2 group enhanced the light harvesting ability compared to the original constructs, which may be attributed to the multiple reflections of light within the porous structure.[36,37]

The charge separation efficiency of CN–NH_2 and CN was assessed using electrochemical impedance spectroscopy (EIS), time-resolved fluorescence (TRPL), and Bode-phase spectroscopy. The contact resistance values are presented in Fig. S21 and S22,† with the Nyquist curve of CN exhibiting a much smaller semicircle compared to CN–NH_2, indicating lower contact resistance for CN. The reduction in contact resistance had a direct impact on significantly improving the charge transfer efficiency, as supported by the electronic lifetimes obtained from time-resolved transient fluorescence decay spectra. The average electronic lifetimes provided a comprehensive reflection of both defect-related nonradiative

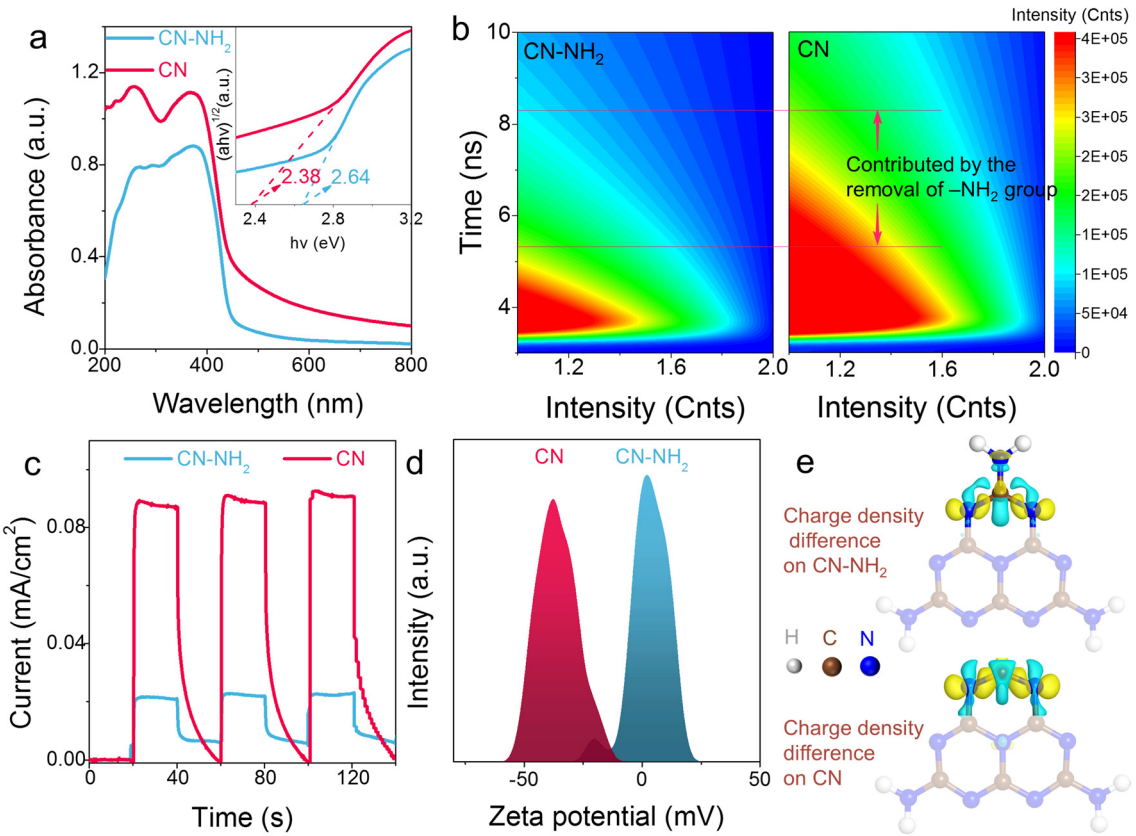

Fig. 4 CN showed superior light harvesting and photoelectric conversion performance, which could enhance the electron density at catalytic sites. a) UV-vis diffuse reflectance spectra. b) Time-resolved fluorescence spectra. c) Transient photocurrent response. d) Zeta potential test. e) The charge density difference (isosurfaces with the yellow zone reflected electron enrichment, while isosurfaces with the green zone reflected the electron depletion).

recombination processes (electron trapping by defects) and radiative recombination processes (excited-state electrons recombining with holes). The average electronic lifetime of CN (6.23 ns) exhibited a 136% increase compared to CN–NH_2 (4.58 ns), indicating a substantial improvement in charge transfer efficiency (Fig. 4b and S23†). Bode-phase spectra further supported this enhanced charge transfer efficiency, with electronic lifetimes of 0.34 and 0.28 μs observed for CN and CN–NH_2, respectively (Fig. S24†). These prolonged excited state lifetimes contributed to the substantially higher photocurrent in transient photocurrent response spectroscopy (Fig. 4c and S25†), as well as enhanced photovoltage (Fig. S26†). All these results indicated that the removal of the –NH_2 group effectively enhanced the electron density at catalytic sites.

The charged characteristics of the samples were further examined by analysing the zeta potential. Zeta potential measurements revealed that CN exhibited a negative charge of −30.73 mV, indicating a higher electronegativity. This negative charge suggests that CN can contribute electrons more easily to activate CO_2 (Fig. 4d). In comparison, CN–NH_2 exhibited a zeta potential of only 0.34 mV. The difference in zeta potential indicates a higher concentration of electrons enriched around the catalytic sites of CN compared to CN–NH_2 (Fig. 4e). This finding highlights the presence of Lewis basic sites on CN, which could contribute electrons to activate CO_2, while the adsorbed CO_2 acts as an electron acceptor. Consequently, the activation of CO_2 relies on the Lewis base/acid interaction between the negatively charged CN and the CO_2 electron acceptor.

As mentioned earlier,[9,32–35] the electron concentration at catalytic sites plays a significant role in the chemisorption and activation of CO_2 molecules, which are crucial steps in CO_2 reduction. To assess the CO_2 chemisorption ability of CN and CN–NH_2, we conducted CO_2 temperature-programmed desorption (CO_2-TPD) analysis. As shown in Fig. 5a, CN exhibited two distinct and intense CO_2-TPD signals, while negligible signals were observed in CN–NH_2, indicating the superior efficiency of CO_2 chemisorption in CN. Furthermore, within CN, the CO_2 chemisorption signal at approximately 427 °C surpassed the signal at around 202 °C, suggesting stronger and more stable chemisorption at higher temperatures. These two signals indicated the presence of two different CO_2 chemisorption sites in CN: the nitrogen atoms adjacent to the –NH_2 group and the nitrogen atoms adjacent to the removed –NH_2 group (Fig. 5a). Importantly, the temperature of the obtained CO_2 chemisorption peak at around 200 °C in CN was slightly lower than that of CN–NH_2, highlighting the crucial role of removing the –NH_2 group at

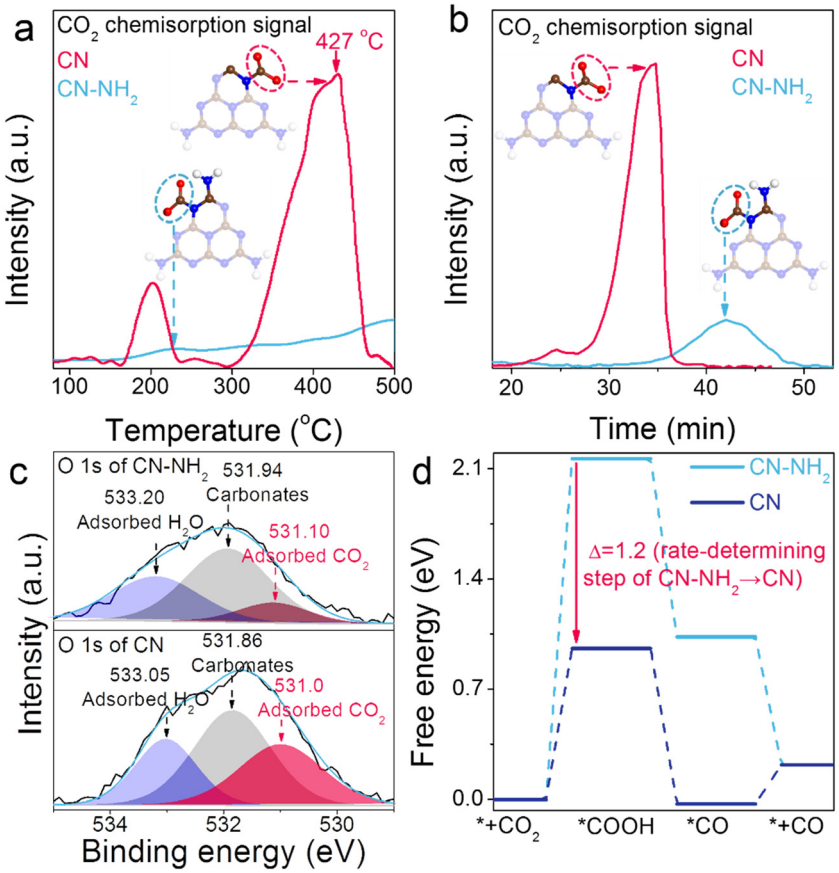

Fig. 5 Electron enrichment at the catalytic sites of CN enhanced the CO_2 chemisorption and activation. a) CO_2 temperature-programmed desorption (CO_2-TPD) for revealing CO_2 chemisorption. b) The collected CO_2 mass spectra during the TPD process (the mass signals were collected at m/z = 44; m/z is the mass to charge ratio). c) XPS of O 1s for revealing CO_2 chemisorption. d) Free energy of CO_2 reduction revealed that CO_2 activation lowered the energy barriers of CO_2 reduction.

the boundary of the CN host. The decomposition temperature of CN (~451 °C) exceeded that of the CO_2 chemisorption signal at ~427 °C, confirming that the latter signal originated from adsorbed CO_2 rather than catalyst decomposition (Fig. S27†). Mass spectrometry analysis of the desorbed CO_2 from CO_2-TPD further supported the conclusion that CN adsorbed a significantly larger quantity of CO_2 (Fig. 5b). XPS analysis of the O 1s region revealed the presence of adsorbed H_2O, carbonates, and adsorbed CO_2 on both CN–NH_2 and CN (Fig. 5c).[38–41] Importantly, the peak area corresponding to adsorbed CO_2 on CN was 3.58 times higher than that on CN–NH_2, underscoring the superior CO_2 chemisorption performance of CN (Fig. 5c and Table S6†). Collectively, these results clearly demonstrated the enhanced CO_2 chemisorption and activation achieved through electron enrichment at catalytic sites.

The activation of CO_2 was evaluated using density functional theory (DFT) calculations, which served to calculate the rate-determining step of CO_2 reduction from CO_2 to *COOH as a standard (Fig. 5d). The energy barrier for this rate-determining step in CN (0.96 eV) was substantially lower compared to CN–NH_2 (2.16 eV), clearly indicating that the electron concentration at catalytic sites significantly reduces the CO_2 activation energy, thus promoting the CO_2 conversion rate under mild conditions.

Taking into account that the higher CO_2 conversion efficiency may be attributed to the larger BET surface area, we have calculated the normalized performance, which is based on the surface area to CO_2 reduction performance (Table S7†), to gain insight into the factors influencing the catalyst. The normalized performance of CN and CN–NH_2 is 5.59 and 8.94 μmol h^{-1} m^{-2}, respectively. This trend rules out the effect of the surface area and further emphasizes the significance of the –NH_2 vacancy in CO_2 adsorption and activation.

Both the higher CO_2 chemisorption and activation abilities will lead to the generation of key intermediates during CO_2 conversion. Hence, we employed *in situ* Fourier-transform infrared (*in situ* FTIR) spectroscopy during CO_2 photoreduction. Interestingly, both CN and CN–NH_2 constructs exhibited the presence of two distinct intermediates, namely *CHO and *CH_3O,[42] which were spectroscopically identified at wavenumbers of 1050 and 1075 cm^{-1}, respectively (Fig. S28†). Notably, a strong bridge-bonded *CO signal was detected in CN–NH_2,[43] while a negligible *CO signal was detected in CN, suggesting that CN could desorb the *CO to produce CO efficiently.

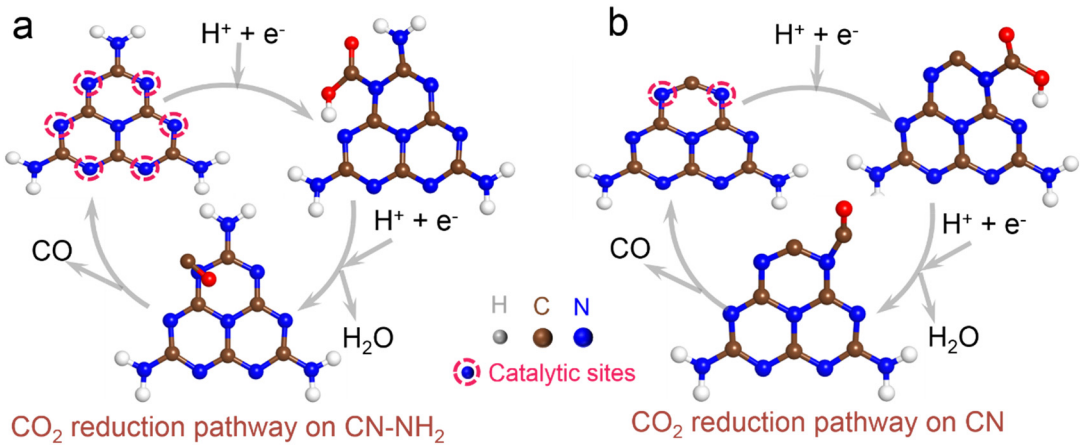

Fig. 6 Density functional theory (DFT) calculation revealing CO_2 reduction pathways on: a) CN–NH_2 and b) CN.

The CO_2 reduction pathways were examined to elucidate the correlation between the efficiency of CO_2 reduction and catalytic sites (Fig. 6a and b). In the case of CN–NH_2, initial adsorption of CO_2 occurred on nitrogen atoms neighbouring the –NH_2 group, followed by a reaction with a proton–electron pair to generate an intermediate species, *COOH. Subsequently, the *COOH species engaged in a further reaction with another proton–electron pair, resulting in the formation of the *CO intermediate and H_2O. Finally, the *CO species were desorbed from the nitrogen atoms adjacent to the –NH_2 group. CN exhibited an analogous CO_2 reduction pathway to CN–NH_2. Notably, only the nitrogen atoms adjacent to the removed –NH_2 group served as catalytic sites in CN, whereas the nitrogen atoms adjacent to the –NH_2 group functioned as catalytic sites in CN–NH_2. Consequently, by considering the disparity in catalytic sites, it was possible to discern the relationship between CO_2 reduction efficiency and catalytic sites. The CO production rates of CN and CN–NH_2 were 58.83 and 18.07 μmol g^{-1} h^{-1}, respectively. Thus, the production rate of CO achieved by CN was 1.00×10^6 μmol $g_{catalytic\ site}^{-1}$ h^{-1}, while CN–NH_2 exhibited a production rate of 4.33×10^4 μmol $g_{catalytic\ site}^{-1}$ h^{-1} for CO (Tables S8 and S9†). Moreover, the turnover number (TON) and turnover frequency (TOF) of CN were 23.11 times higher than those of CN–NH_2 (Table S10†). These findings collectively suggested that the modulation of the –NH_2 group enhanced the efficiency of CO_2 reduction.

Conclusions

In this study, we successfully fabricated a carbon nitride material with partially removed –NH_2 groups (referred to as CN). Remarkably, CN exhibited superior light harvesting and photoelectric conversion capabilities compared to CN–NH_2, leading to higher electron population enrichment at catalytic sites. This electron enrichment at catalytic sites played a pivotal role in enhancing the chemisorption and activation of CO_2, effectively lowering the energy barrier associated with CO_2 reduction. As a result of the enhanced CO_2 chemisorption and activation, CN demonstrated exceptional photocatalytic performance surpassing CN–NH_2. This investigation not only emphasized the significance of CO_2 chemisorption and activation through catalytic site modulation, but also established a promising avenue for the development of novel catalysts aimed at boosting CO_2 reduction.

Author contributions

Debin Zeng: resources, software, methodology, validation, writing-original draft, and writing-review & editing. Xiting Wang: software. Chunguang Kuai: software. Zhuo Jiang: conceptualization, methodology, validation, and writing-review & editing. Yuzheng Guo: conceptualization, methodology, validation, and writing-review & editing.

Conflicts of interest

There are no conflicts to declare.

Acknowledgements

This work was supported by the National Key Research and Development Program of China (2022YFA1502902) and the National Natural Science Foundation of China (No. 62174122, No. 22101217). The numerical calculations in this article were done on the supercomputing system in the Supercomputing Center of Wuhan University.

References

1 Y. L. Chen, Y. Qu, X. Zhou, D. Z. Li, P. Xu and J. M. Sun, *ACS Appl. Mater. Interfaces*, 2020, **12**, 41527–41537.
2 Y. L. Chen, X. Q. Liu, L. Hou, X. R. Guo, R. W. Fu and J. M. Sun, *Chem. Eng. J.*, 2020, **383**, 123132.
3 Y. L. Chen, Y. Qu, P. Xu, X. Zhou and J. M. Sun, *J. Colloid Interface Sci.*, 2021, **601**, 326–337.
4 K. Maeda, K. Sekizawa and O. Ishitani, *Chem. Commun.*, 2013, **49**, 10127–10129.

5 Y. Yamazaki, H. Takeda and O. Ishitani, *J. Photochem. Photobiol., C*, 2015, **25**, 106–137.
6 K. E. Dalle, J. Warnan, J. J. Leung, E. Reuillard, I. S. Karmel and E. Reisner, *Chem. Rev.*, 2019, **119**, 2752–2875.
7 A. E. Green, J. Justen, W. Schöllkopf, A. S. Gentleman, A. Fielicke and S. R. Mackenzie, *Angew. Chem.*, 2018, **130**, 15038–15042.
8 J. M. Weber, *Int. Rev. Phys. Chem.*, 2014, **33**, 489–519.
9 Y. H. Cao, L. Guo, M. Dan, D. E. Doronkin, C. Q. Han, Z. Q. Rao, Y. Liu, J. Meng, Z. A. Huang, K. B. Zheng, P. Chen, F. Dong and Y. Zhou, *Nat. Commun.*, 2021, **12**, 1675.
10 X. C. Wang, K. Maeda, A. Thomas, K. Takanabe, G. Xin, J. M. Carlsson, K. Domen and M. Antonietti, *Nat. Mater.*, 2009, **8**, 76–80.
11 R. R. Wang, P. J. Yang, S. B. Wang and X. C. Wang, *J. Catal.*, 2021, **402**, 166–176.
12 G. C. Huang, Q. Niu, J. W. Zhang, H. M. Huang, Q. S. Chen, J. H. Bi and L. Wu, *Chem. Eng. J.*, 2022, **427**, 131018.
13 G. J. Chen, F. Wei, Z. R. Zhou, B. Su, C. Yang, X. F. Lu, S. B. Wang and X. C. Wang, *Sustainable Energy Fuels*, 2023, **7**, 381–388.
14 G. J. Chen, Z. R. Zhou, B. F. Li, X. H. Lin, C. Yang, Y. X. Fang, W. Lin, Y. D. Hou, G. G. Zhang and S. B. Wang, *J. Environ. Sci.*, 2023, DOI: **10.1016/j.jes.2023.05.028**.
15 W. Chananchana, P. Nuengmatcha and S. Chanthai, *Orient. J. Chem.*, 2017, **33**, 2920.
16 H. W. Gu, Y. B. Guo, S. Y. Wong, Z. Zhang, X. P. Ni, Z. X. Zhang, W. X. Hou, C. B. He, V. P. W. Shim and X. Li, *Microporous Mesoporous Mater.*, 2013, **170**, 226–234.
17 G. Kresse and D. Joubert, *Phys. Rev. B: Condens. Matter Mater. Phys.*, 1999, **59**, 1758.
18 G. Kresse and J. Furthmüller, *Comput. Mater. Sci.*, 1996, **6**, 15–50.
19 J. P. Perdew, J. A. Chevary, S. H. Vosko, K. A. Jackson, M. R. Pederson, D. J. Singh and C. Fiolhais, *Phys. Rev. B: Condens. Matter Mater. Phys.*, 1992, **46**, 6671.
20 J. P. Perdew and K. Burke, *Phys. Rev. Lett.*, 1996, **77**, 3865.
21 Z. A. Lan, G. G. Zhang and X. C. Wang, *Appl. Catal., B*, 2016, **192**, 116–125.
22 Y. Y. Kang, Y. Q. Yang, L. C. Yin, X. D. Kang, L. Z. Wang, G. Liu and H. M. Cheng, *Adv. Mater.*, 2016, **28**, 6471–6477.
23 S. E. Guo, Z. P. Deng, M. X. Li, B. J. Jiang, C. G. Tian, Q. J. Pan and H. G. Fu, *Angew. Chem.*, 2016, **128**, 1862–1866.
24 G. Q. Li, N. Yang, W. L. Wang and W. F. Zhang, *J. Phys. Chem. C*, 2009, **113**, 14829–14833.
25 J. J. Chen, Z. Y. Mao, L. X. Zhang, D. J. Wang, R. Xu, L. J. Bie and B. D. Fahlman, *ACS Nano*, 2017, **11**, 12650–12657.
26 W. N. Xing, W. G. Tu, M. Ou, S. Y. Wu, S. M. Yin, H. J. Wang, G. Chen and R. Xu, *ChemSusChem*, 2019, **12**, 2029–2034.
27 W. Liu, C. J. Song, M. P. Kou, Y. Y. Wang, Y. Deng, T. Shimada and L. Q. Ye, *Chem. Eng. J.*, 2021, **425**, 130615.
28 M. H. Liu, C. G. Wei, H. Y. Zhuzhang, J. M. Zhou, Z. M. Pan, W. Lin, Z. Y. Yu, G. G. Zhang and X. C. Wang, *Angew. Chem., Int. Ed.*, 2022, **61**, e202113389.
29 C. D. Lv, Y. M. Qian, C. S. Yan, Y. Ding, Y. Y. Liu, G. Chen and G. H. Yu, *Angew. Chem.*, 2018, **130**, 10403–10407.
30 Y. H. Li, M. L. Gu, X. M. Zhang, J. J. Fan, K. L. Lv, S. A. C. Carabineiro and F. Dong, *Mater. Today*, 2020, **41**, 270–303.
31 F. Y. Liu, Y. Tong, C. F. Li and X. L. Liu, *J. Phys. Chem. Lett.*, 2021, **12**, 10359–10365.
32 H. Li, B. C. Zhu, S. W. Cao and J. G. Yu, *Chem. Commun.*, 2020, **56**, 5641–5644.
33 Y. Y. Sun, G. H. Li, W. Sun and X. X. Zhou, *J. CO_2 Util.*, 2023, **67**, 102344.
34 U. J. Etim, C. C. Zhang and Z. Y. Zhong, *Nanomaterials*, 2021, **11**, 3265.
35 L. L. Lin, K. Wang, K. Yang, X. Chen, X. Z. Fu and W. X. Dai, *Appl. Catal., B*, 2017, **204**, 440–455.
36 D. B. Zeng, X. T. Wang, Y. S. Liu, D. M. Liu, Z. Y. Zhang, L. F. Fei, J. Robertson, C. G. Kuai and Y. Z. Guo, *ACS Sustainable Chem. Eng.*, 2022, **10**, 5758–5769.
37 D. B. Zeng, L. T. Wang, R. A. Du, Z. Wu, X. T. Wang, C. G. Kuai, Y. Z. Guo and C. L. Yu, *Mater. Chem. Phys.*, 2023, 128021.
38 M. Favaroa, H. Xiao, T. Cheng, W. A. Goddard III, J. Yano and E. J. Crumlin, *Proc. Natl. Acad. Sci.*, 2017, **114**, 6706–6711.
39 X. Y. Deng, A. Verdaguer, T. Herranz, C. Weis, H. Bluhm and M. Salmeron, *Langmuir*, 2008, **24**, 9474–9478.
40 C. Zhang, M. Y. Zhang, Y. Li and D. M. Shuai, *Appl. Catal., B*, 2019, **248**, 11–21.
41 B. Eren, C. Heine, H. Bluhm, G. A. Somorjai and M. Salmeron, *J. Am. Chem. Soc.*, 2015, **137**, 11186–11190.
42 X. D. Li, Y. F. Sun, J. Q. Xu, Y. J. Shao, J. Wu, X. L. Xu, Y. Pan, H. X. Ju, J. F. Zhu and Y. Xie, *Nat. Energy*, 2019, **4**, 690–699.
43 T. Wang, L. Chen, C. Chen, M. T. Huang, Y. J. Huang, S. J. Liu and B. X. Li, *ACS Nano*, 2022, **16**, 2306–2318.